Advances in Aerodynamics

RESEARCH Open Access

Hypersonic aerodynamic force balance using temperature compensated semiconductor strain gauges

Huacheng Qiu[1*], Yanguang Yang[2], Peng Sun[1], Genming Chao[1], Yousheng Wu[1] and Yingdong Chen[1]

*Correspondence: qiuhuacheng@cardc.cn

[1] Hypervelocity Aerodynamics Institute, China Aerodynamics Research and Development Center, Mianyang 621000, China
[2] China Aerodynamics Research and Development Center, Mianyang 621000, China

Abstract

Metal foil strain gauges remain the state-of-the-art transducers for wind tunnel balances. While strain gauge technology is very mature, piezoresistive semiconductor sensors offer alternatives that are worth exploring to assess their unique benefits, such as better strain resolution and accuracy, which would enable balances to be designed with higher factors to safety and hence longer fatigue lifetimes. A new three-component balance, based on temperature compensated semiconductor strain gauges, is designed, calibrated and tested in a hypersonic low density wind tunnel. The static accuracy of the semiconductor balance is calibrated better than 0.3% FS, and the dynamic accuracy of the balance is established using a HB-2 standard model in a Mach 12 hypersonic flow. Good experimental repeatability is confirmed to be better than 2.5% FS, and the effectiveness of the balance is demonstrated by comparing the forces and moments of measured data with computational fluid dynamics simulations, as well as reference wind tunnel results under similar conditions.

Keywords: Hypersonic flow, Aerodynamic force balance, Semiconductor strain gauge, Temperature compensation

1 Introduction

Reliable and robust aerodynamic force measurement instruments are required in wind tunnel experiments. A force balance is a precision-machined instrument that is capable of accurately and precisely measuring the aerodynamic loads imparted on the aircraft model, by applying strain gauges at strategic locations to measure the strain due to applied loads. While there is no urgent need to replace balance mechanical structures [1], the time is surely right to consider new strain sensing technologies for an upgraded generation of force balances to satisfy ever more demanding requirements in the new future.

Metal foil strain gauges remain the state-of-the-art transducers for wind tunnel balances. They offer a compelling combination of resolution (less than 1 microstrain (με)), long term stability, and temperature stability [2]. While strain gauge technology is very mature, other sensor technologies offer alternatives that are worth exploring to assess the unique benefits they may offer to address researcher needs. Readers can refer to several

papers [3–7] for alternative strain sensing technologies that could replace or complement metal foil strain gauges. In this work, we focus on the piezoresistive semiconductor strain gauge technology. Unlike a metal foil strain gauge, whose change in resistance is primarily linked to geometrical changes, semiconductor gauge exhibits greater sensitivity, larger bandwidths and shorter response time, making them well suited for precise or dynamic measurements [8].

1.1 Brief history of strain gauge development

The measurement of strain is important in numerous applications in science and engineering, and metal foil strain gauges are widely used. The measurement principle is based on the change in electrical conductance and geometry of a stretched conductor. William Thomson first reported on the change in resistance with elongation in iron and copper in 1857 [9]. Motivated by that work, Tomlinson confirmed this strain-induced change in conductivity and made measurements of temperature and direction dependent elasticity and conductivity of metals under varied orientations of mechanical loads and electrical currents (Fig. 1) [10, 11]. Higson reviewed the development history of metal foil strain gauges, from their introduction in 1938 to 1964 [12].

In field strain tests, the measuring structure and the resistive element of the strain gauge have linear expansion coefficients. The strain gauge bonded on the surface of the measuring structure provides a thermally-induced apparent strain. Self-temperature-compensation strain gauges are designed to adjust the resistive temperature coefficient

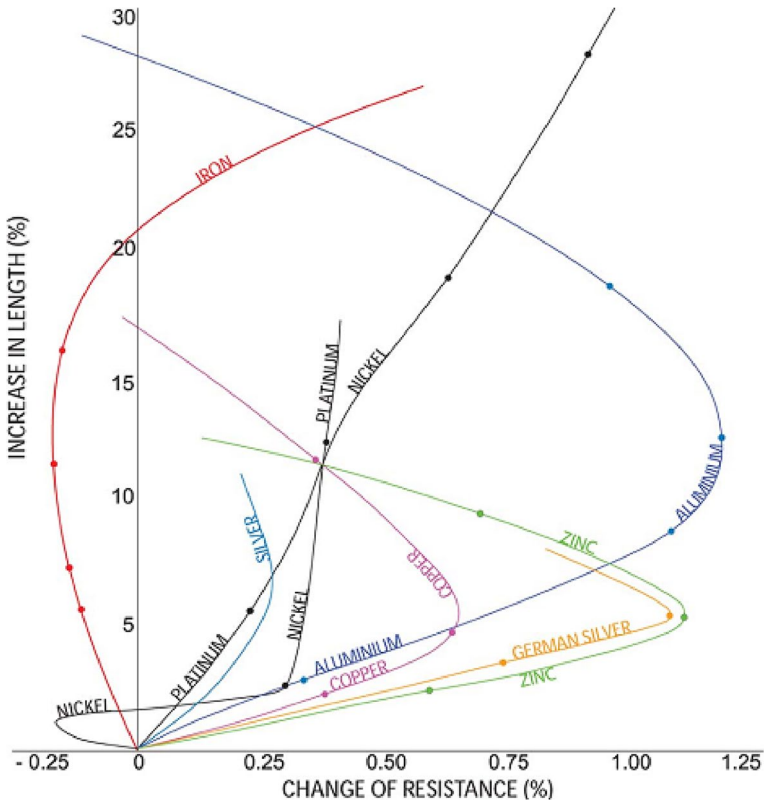

Fig. 1 The change of resistance produced in different metals by hammering-induced strain [10, 13]

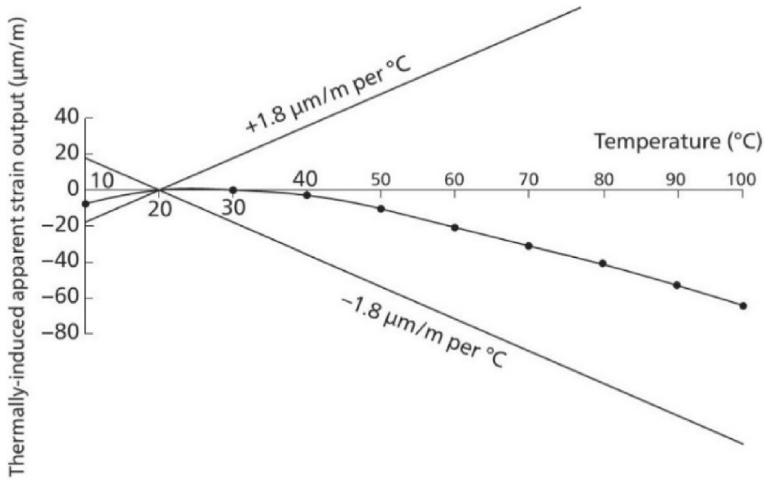

Fig. 2 Typical temperature characteristics of self-temperature-compensation metal foil strain gauges in Kyowa [14]

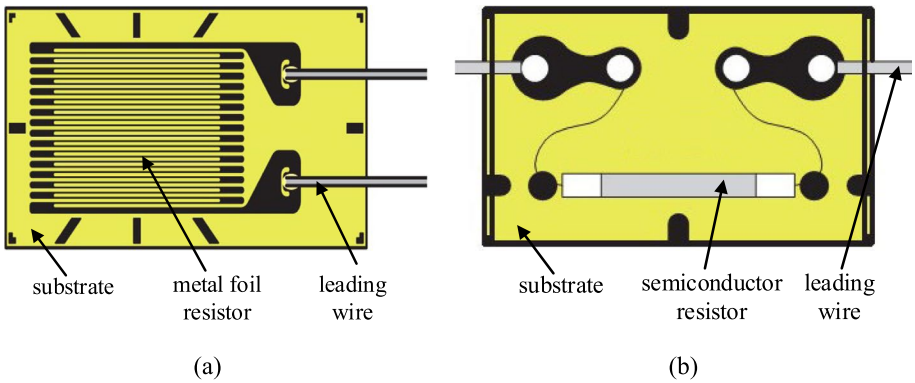

Fig. 3 Sketches of **a** metal foil strain gauge and **b** semiconductor strain gauge

of their resistive elements to match the linear expansion coefficient of the measuring objects, in order to get thermally-induced apparent strain close to zero. For example, Kyowa's SELCOM gauges [14] have been adjusted so that, when they are bonded to suitable measured materials, the average value of the apparent strain in the self-temperature-compensation range is within ± 1.8 μm/m per ℃. Figure 2 shows the apparent strain output of its strain gauges.

Developed in the 1950s as an outgrowth of work performed at Bell Laboratories on semiconductor devices for the electronics industry, semiconductor strain gauges were first described and popularized by Smith [15] and Mason et al. [16]. Unlike metal foil strain gauges (typical structure refers to Fig. 3a), semiconductor gauges (Fig. 3b) work on the principle of piezoresistance. Kulite Semiconductor and Microsystems developed commercial products in the late 1950s [17]. The gauges were bonded to metal flexural structures to make pressure sensors, load cells and accelerometers.

1.2 Semiconductor strain gauge

Unlike a metal foil strain gauge, whose change in resistance is primarily linked to geometrical changes, semiconductor strain gauges exhibit greater sensitivity (gauge factor > 100) [4], and the strain resolution less than 0.1 με can be expected [13]. While semiconductor based gauges are inherently brittle, manufactures typically guarantee their gauges to 3500 με in tension [18]. High strain sensitivity, rock-solid repeatability, and impressive reliability are the hallmark characteristics of semiconductor gauges; these very features make them the only choice for certain measurement problems, particularly for applications involving low strains, or high cycles, or very long (kilometers) lead wires. Additionally, since the gauges are single-crystal elements, they have no measurable hysteresis or creep, which makes them attractive for long-term installations.

A semiconductor gauge's change in resistance is affected by the average number of charge carriers and the average carrier mobility of the semiconductor [13], which means the gauge is also sensitive to temperature variations. In many cases, the resistance change due to temperature is higher than that of the desired signal. Compensation techniques must be carried out since they are more sensitive to temperature than foil gauges.

A six-component wind tunnel balance using semiconductor strain gauges was produced in Military Technical Institute (VTI), Serbia [19–21]. The balance was designed specifically for high drag models requiring large starting and stopping loads. These tests were tens of seconds in duration and produced a small temperature change of approximately 1℃. The researchers concluded the balance worked well for this application, but they speculated that it would not be generally used, especially in wide temperature range. NASA Ames Research Center [22, 23] carried out direct measurements of skin friction in hypersonic impulsive scramjet experiments, based on a balance using semiconductor strain gauges. The balance measured the wall shear stress in the range of 450–1320 Pa in a scramjet flowfield at Mach 12–16 in a shock tunnel. Further, in order to minimize the effect of temperature, the cavity surrounding the gauges was filled with silicon oil. The Institute of Theoretical and Applied Mechanics in Russia [24] reported a miniature skin-friction semiconductor balance, which provided high sensitivity (≤ 10 g) and the necessary high frequency response. Again, the internal volume of the balance housing was sealed with oil, to protect the gauges from the thermal effect of gases at tests in a high-enthalpy wind tunnel.

1.3 Content in this work

In hypersonic wind tunnel experiments, the flow gas needs to be heated to elevated temperatures and this generates heating of the aircraft and, hence, the balance and strain gauges located inside. Temperature influence becomes an important issue, and careful compensation for the temperature effect is necessary in this case. Otherwise, the error caused by temperature variations would cover the advantage of high strain sensitivity of the balance, and lead to very unreliable results.

This paper presents a three-component internal balance using a novel semiconductor strain gauge, which has an on-chip full Wheatstone bridge configuration, and an external compensation circuit, for fine compensation of temperature effect. Static calibrations and Mach 12 wind tunnel experiments have been carried out. In order to quantify the measured

aerodynamic coefficients, the experimental results are compared with computational fluid dynamics (CFD) simulations, as well as reference wind tunnel results under similar conditions.

2 Semiconductor balance

Compared to metal foil strain gauges that respond only to changes in geometry, semiconductor strain gauges exhibit up to two orders-of-magnitude greater sensitivity. The foremost disadvantages associated with semiconductor sensors are high temperature sensitivity and poor long-term stability. The elimination of these artefacts requires a more complicated conditioning circuit than metal foil strain gauges.

2.1 Strain sensitivity of semiconductor strain gauge

As shown in Fig. 4, a typical semiconductor strain gauge consists of a planar p-doped resistor with heavily p^+ doped contacts. When the gauge is elongated in the x-axis, the electric conductivity (mobility and numbers of holes and electrons) decreases in that direction, and the resistance increases.

The electrical resistance (R) of a homogeneous structure is a function of its dimensions and resistivity (ρ):

$$R = \frac{\rho l}{a}, \tag{1}$$

where l is the length, and a is the average cross-sectional area.

The change in resistance $\Delta R/R$ due to applied stress is a function of geometry effects $(1+2\nu)$ and resistivity changes $(\Delta\rho/\rho)$ of the material:

$$\frac{\Delta R}{R} = (1+2\nu)\varepsilon + \frac{\Delta\rho}{\rho} = (1+2\nu+\pi E)\varepsilon. \tag{2}$$

The gauge factor (GF) is then:

$$GF = \frac{\Delta R/R}{\varepsilon} = 1+2\nu+\pi E, \tag{3}$$

where π is the piezoresistive coefficient and E is the elasticity modulus of the material.

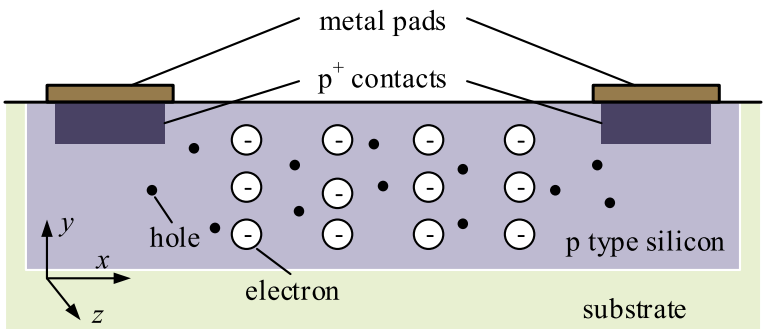

Fig. 4 A cross-section of a semiconductor strain gauge

The cross-sectional area of a bulk material reduces in proportion to the longitudinal strain by its Poisson's ratio, ν, which ranges from 0.20 to 0.50 for most metals, and 0.06 to 0.36 for semiconductive silicon [25, 26]. Geometrical effects alone provide a *GF* of approximately 1.4 to 2.0, and the change in πE, for a metal is small — on the order of 0.3. However, for semiconductive silicon, $\pi = (40 \sim 80) \times 10^{-11}$ m^2/N, $E = 1.76 \times 10^{11}$ Pa [27], and πE is 50 ~ 100 times larger than the geometric term $1 + 2\nu$. So the *GF* for the semiconductor strain gauge is:

$$GF = \pi E \approx 70 \sim 140. \tag{4}$$

2.2 Temperature sensitivity and compensation technique

It is well documented that semiconductive resistors are highly sensitive to temperature and need to be calibrated over a wide temperature range in order to ensure accurate strain predictions. Figure 5a shows an apparent strain output VS temperature of a typical semiconductive resistor. This figure shows that this resistor has a positive temperature coefficient of resistance (TCR), and its response to temperature is an order of magnitude ($\approx 17\times$) greater than the gauge response to applied strain.

Furthermore, the gauge factor decreases with temperature for the semiconductive resistors. Much of the drop in sensitivity with increased temperature is the result of the large, positive TCR of semiconductive silicon, causing the gauge resistance (R) to increase significantly, thus decreasing the apparent sensitivity ($\Delta R/R$). Figure 5b shows the gauge factor curve for the semiconductive resistor varying with different temperatures.

In many cases, the resistance change due to temperature is higher than that of the desired signal. The most common temperature compensation techniques in the semiconductor strain gauge use identical resistors in a Wheatstone bridge configuration. Co-fabricated resistors of the same design exhibit similar temperature dependence; besides, a tunable resistor R_0 is also placed in the bridge to precisely adjust the balance of the bridge. Therefore, the zero output of a compensated Wheatstone bridge remains constant with temperature changes.

Since all semiconductor gauges have a positive TCR and a negative temperature coefficient (TC) of gauge factor, the change of gauge factor with temperature can be compensated by increasing the bridge supply voltage in proportion to the loss in sensitivity. This is accomplished by inserting low-TCR, fixed resistors *Rs* in series with bridge power

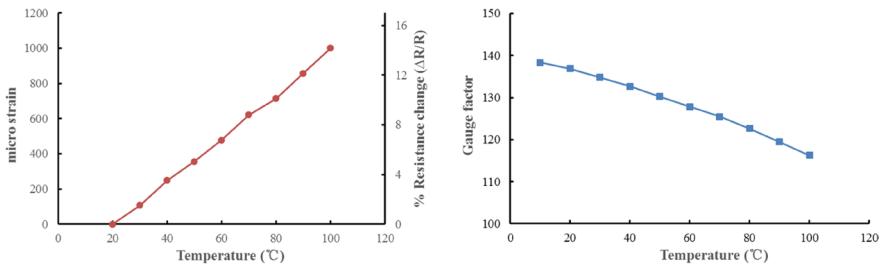

(a) (b)

Fig. 5 **a** Apparent strain and **b** gauge factor versus temperature

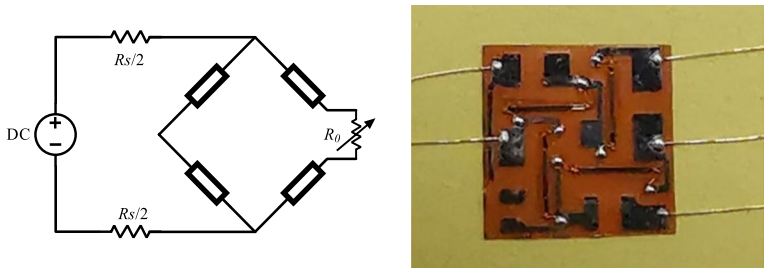

Fig. 6 **a** Schematic circuit of temperature compensation for **b** the semiconductor strain gauge

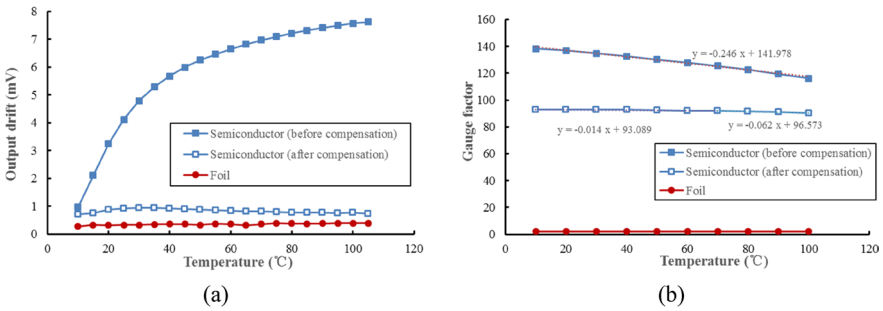

Fig. 7 **a** Output drift and **b** gauge factor variations of the semiconductor strain gauge before and after temperature compensation, as well as those of foil strain gauge

leads. In this circuit, the bridge is considered as a single, variable resistor with a positive TCR, and the circuit acts like a voltage divider. By choosing the ratio of series resistance to bridge resistance equal to the ratio of bridge TCR to TC of gauge factor, the increase in bridge voltage resulting from the positive bridge TCR can be made to offset the drop in bridge sensitivity caused by the negative TC of gauge factor. It is a usual practice to insert one-half of *Rs* into each of the two power leads, although this is not a requirement.

The schematic of temperature compensation circuit (Fig. 6a) for the semiconductor strain gauge (Fig. 6b) is shown below.

The variations of the output drift and the gauge factor with temperature of the semiconductor strain gauge before and after compensation are shown in Figs. 7a and b, and those of metal foil strain gauges are also shown drawn for comparison.

As can be seen from Fig. 7a, in the temperature range of 10 ~ 100℃, the output drift of the semiconductor strain gauge without temperature compensation is about 7 mV, and it reduces to 0.25 mV after compensation. The drift of metal foil strain gauge is about 0.1 mV. The compensation technique reduces the output drift of the semiconductor strain gauge by about 30 times, which is only about 2.5 times that of the foil gauge.

From Fig. 7b one can find that, as temperature increases, the gauge factor of the semiconductor strain gauge decreases with a coefficient of −0.246/℃ before compensation. The coefficient reduces to −0.014/℃ (10 ~ 70℃) and −0.062/℃ (70 ~ 100℃) after compensation. Although the compensation reduces the gauge factor of the semiconductor strain gauge from 138 (@ 10℃) to 92, it is still much higher than that of the foil counterpart, which is about 2.

2.3 Semiconductor balance configuration

Based on the new developed semiconductor strain gauges, a three-component semiconductor balance was fabricated. The gauges were installed on the balance by means of adhesive, and the surface of the gauge was coated with epoxy resin and silica gel, to isolate any external environment interferences such as humidity and light (Fig. 8a). Twelve semiconductor gauges were arranged on the flexural beams of the balance, to convert

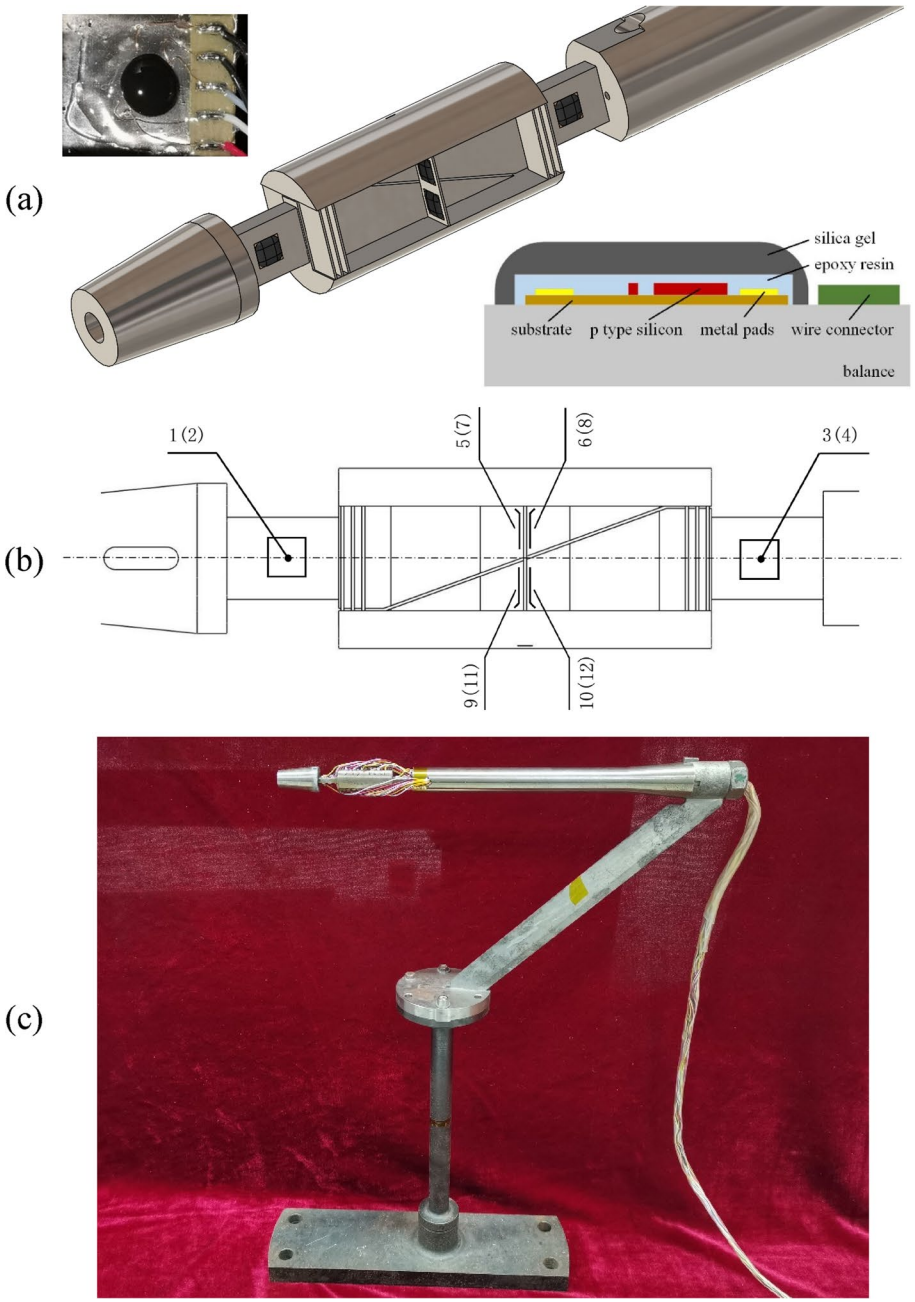

Fig. 8 Three-component semiconductor balance: **a** drawing of the balance, with a photo of the gauge after installation in the upper left, and a sketch of the installation in the lower right, **b** diagram of the balance marked with positions of the gauges, and **c** overall photo of the balance

Table 1 Calibration performance of the semiconductor balance

	F_A	F_N	*Mz*
Designed load	800 g	800 g	2400 g·mm
Designed strain	50 με	50 με	50 με
Zero drift (30 min)	0.01% FS	0.07% FS	0.08% FS
Hysteresis creep (30 min)	0.15% FS	0.11% FS	0.10% FS
Repeatability precision	0.06% FS	0.09% FS	0.16% FS
Accuracy	0.21% FS	0.17% FS	0.29% FS

Fig. 9 The Φ0.3 m hypersonic low density wind tunnel

the strain (and hence, the applied aerodynamic loads) to electrical outputs, as depicted in Fig. 8b, where the axial force (F_A) was measured by the gauges 5 – 12, the normal force (F_N) and the pitching moment (Mz) were measured by the gauges 1 – 4. Figure 8c shows a photo of the balance used in this work.

2.4 Balance static calibration

A force balance needs a careful calibration before wind tunnel experiments. Table 1 shows the calibration performance of the semiconductor balance. The repeatability precisions of all components are better than 0.2% FS, and the accuracies are better than 0.3% FS, which reach the qualified indicators stipulated in the national standard [28].

3 Experimental procedure

The aerodynamic force measurements were carried out in the Φ0.3 m hypersonic low density wind tunnel in China Aerodynamics Research and Development Center. This tunnel is a blowdown wind tunnel consisting of an expansion nozzle with a large expansion ratio, a vacuum chamber as a test section, and a vacuum pumping system to allow operation at low ambient pressure. It is possible to accelerate the test gas to a high Mach number between 5 and 24. Figure 9 shows an overall view of the wind tunnel.

Tunnel model was supported by a tail sting mounted on a pitch apparatus in the test section, as shown in Fig. 10. A Hypervelocity Ballistic correlation model 2 (HB-2) model was used in this work, all dimensions of the model are defined in terms of the forebody

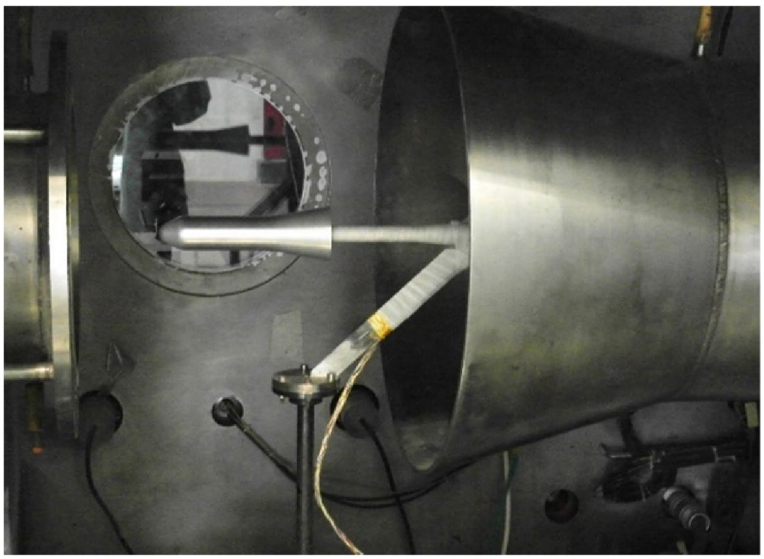

Fig. 10 HB-2 model in the test section

Table 2 Wind tunnel operating parameters

Ma	T_0 (K)	P_0 (MPa)	*Re* ($\times 10^5$)	AoA (°)	Flow medium
12.7	600	2.0	4.44	−4°~8°	N_2

diameter $D=40$ mm, and the angle of attack (AoA) was set from −4° to +8°, with a stepwise way of 2°.

In Table 2, the operating parameters of the tunnel are tabulated. A nominal Mach 12 nozzle was used in this experiment, and the freestream Mach number *Ma* was calibrated to be 12.7. The average stagnation temperature T_0 and pressure P_0 were 600 K and 2.0 MPa respectively, the unit Reynolds number Re_L was calculated to be 2.26×10^6/m, and the Reynolds number *Re* based on the model length was 4.44×10^5. In order to prevent gas condensation, dry pure nitrogen was used as the flow medium.

4 Experimental results

For the wind tunnel experiments, the three-component balance outputs corresponding to the total axial force F_A, normal force F_N, and pitching moment *Mz* were converted to the aerodynamic coefficient C_A, C_N and C_{Mz}, by dividing the dynamic pressure and reference area $S=0.001257$ m^2, as well as the reference length $L=0.196$ m for the pitching moment coefficient.

Eight wind tunnel runs have been performed. Tables 3 and 4 were the averaged operation parameters and measured aerodynamic coefficient repeatability, respectively.

In the wind tunnel experiments, the HB-2 model was set into the hypersonic flow field after the flow became stable, the nominal AoA was increased in a stepwise way from −4° to +8° in an interval of 2°. Figure 11 shows the output signal of the semiconductor balance during one wind tunnel run over a 200 s test period.

Table 3 Averaged operation parameters of the eight wind tunnel runs

	Run 1	Run 2	Run 3	Run 4	Run 5	Run 6	Run 7	Run 8
T_0 (K)	598	598	599	598	599	599	599	598
P_0 (MPa)	1.980	2.002	2.020	2.030	2.018	2.000	2.000	2.030

Table 4 Measured aerodynamic coefficient repeatability of the eight wind tunnel runs

C_A	C_N	C_{Mz}	*Xcp*
2.39% FS	1.16% FS	1.45% FS	±0.0025

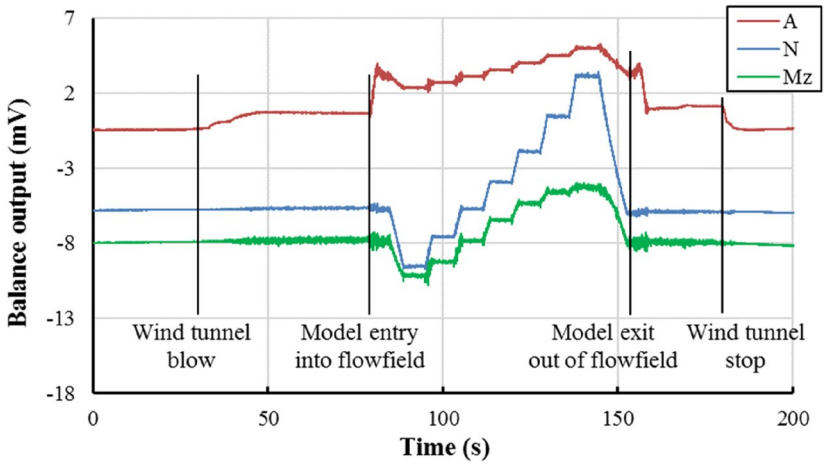

Fig. 11 Balance output during wind tunnel run

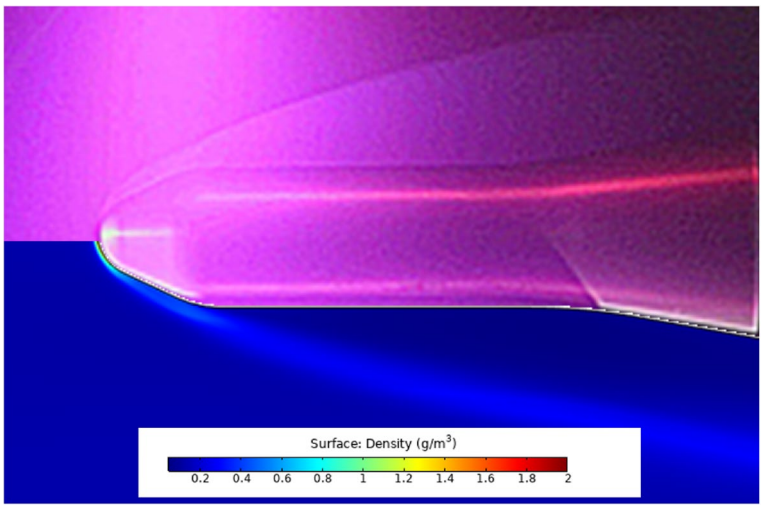

Fig. 12 Flow visualization results of the HB-2 model: glow discharge image (upper), and CFD simulated density contour (lower)

Figure 12 shows a flow visualization image of the HB-2 standard model of 0° AoA, using glow discharge technology [29]; as a comparison, the result of the laminar computational fluid dynamics (CFD) simulation under the experimental condition is also presented. In hypersonic rarefied flows, traditional optical visualization technologies, such as shadowgraph, schlieren and interferometric methods are no longer applicable, due to low density of the flow stream. In the present experiments, a high frequency AC electric power was used to excite glow plasma in the flowfield. The intensity of the plasma depends on the density of the gas and can be photographed as flow visualization. The CFD simulation was implemented by the commercial software CFD++, the grid size was ca. 0.1 million, and the first cell height was 10 μm, to ensure the non-dimensional wall distance y^+ approaches the order of 1; adiabatic wall and non-slip conditions were imposed on the HB-2 model surface. The experimental image and the CFD density contour were found to be in good agreement.

The comparison results of the aerodynamic coefficients between the experiments and CFD simulations, as well as reference results measured from the Φ1 m hypersonic low density wind tunnel (FD17A) under the condition of $Ma = 12.33$, $P_0 = 9.372$ MPa, $T_0 = 1300$ K, and $Re = 2.77 \times 10^6$, are illustrated in Fig. 13. The error bars show the standard deviation of the eight wind tunnel runs. It can be seen that the experimental results generally agree well with the CFD predictions and the reference FD17A wind tunnel results.

The repeatability of the C_A measurements was not good as other components, and the main reason was suspected to be the temperature gradient effect. The axial component as a whole, being a parallelogram construction with a model at the front

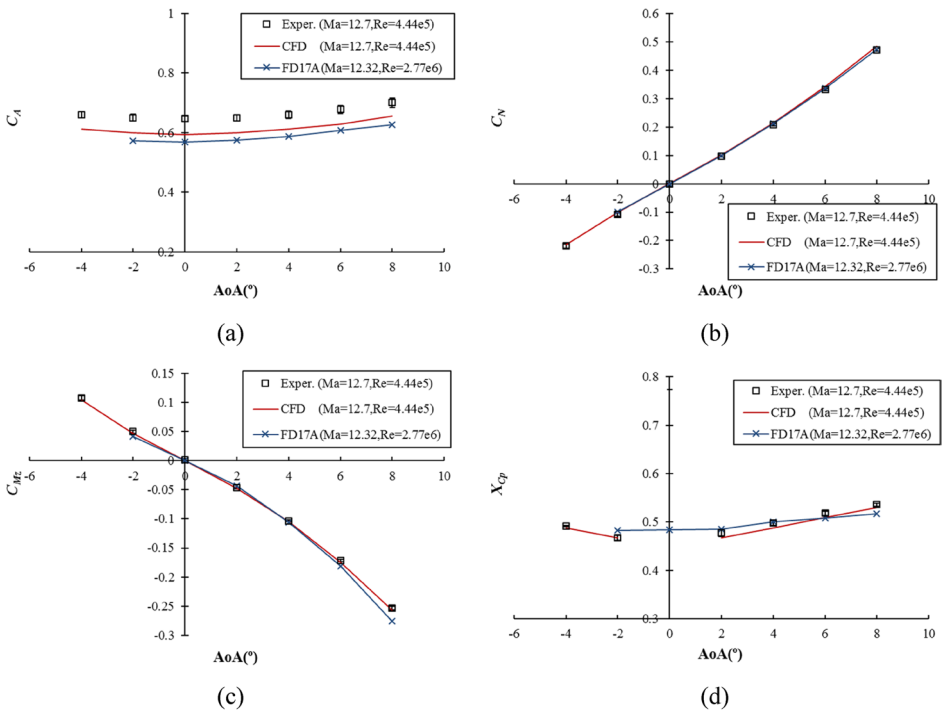

Fig. 13 Comparisons of aerodynamic coefficients, **a** C_A, **b** C_N, **c** C_{Mz} and **d** X_{cp}. Error bars show the standard deviation of the eight runs

and a sting at the rear, is significantly affected by temperature gradient during hypersonic flow blows. That is, (1) varying temperatures on the parallelogram beam will cause the beam to bend and thus produce real strain; (2) the full Wheatstone bridge on the semiconductor strain gauge will produce output drift due to inhomogeneous temperatures.

The C_A was also found to be different from the CFD prediction or the FD17A measurement. For hypersonic rarefied aerodynamics, the accuracy of axial force prediction is generally poor, which may relate to model temperature, wall slip, viscosity effects, etc. In order to accurately predict the C_A value, it is necessary to suppress the temperature gradient effect of the axial force element of the balance, as well as accurately simulate the wall temperature ratio of the model.

For hypersonic wind tunnel aerodynamic experiments, the measurement accuracy is affected by model fabrication, balance calibration, wind tunnel operation, data acquisition and processing, etc., but the main error comes from the non-uniformity of the wind tunnel flowfield [30, 31]. The influence of flowfield non-uniformity on the aerodynamic coefficients is relatively complex. In order to simplify the analysis, only the influence of the axial gradient of the Mach number is considered. The results are shown in Fig. 14, where the average Mach number in the uniform area of the flowfield was used for the experiments, and the Mach numbers at the head and tail positions of the model were used for the head limit and tail limit, respectively. The deviation between the two limits was about 3.73%.

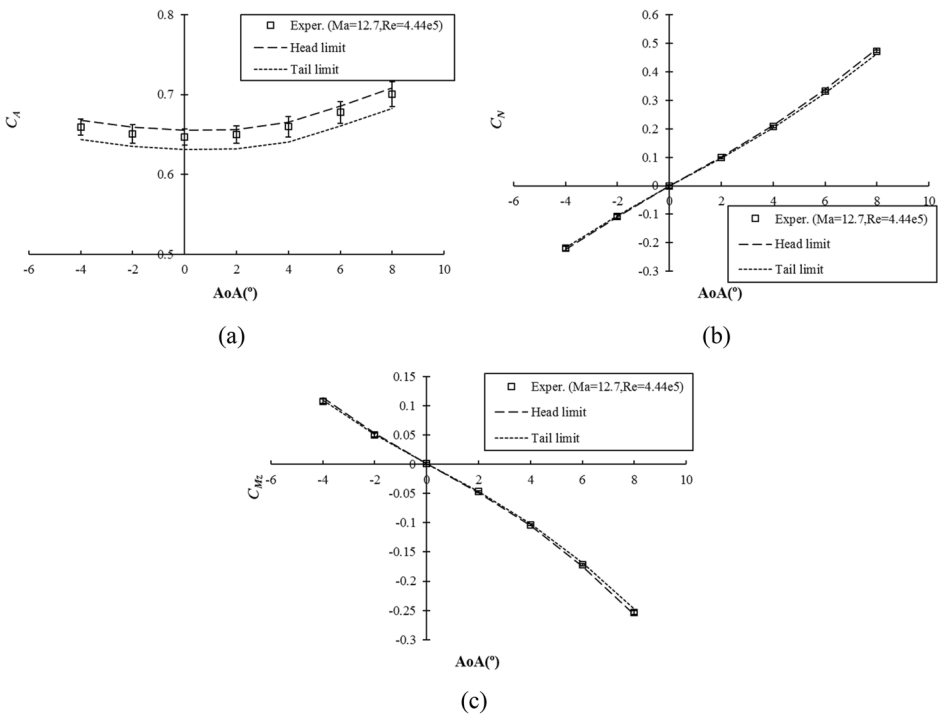

Fig. 14 The influence of flowfield non-uniformity on the aerodynamic coefficients, **a** C_A, **b** C_N, and **c** C_{Mz}

5 Conclusion

In this work, a novel force balance based on temperature compensated semiconductor strain gauges was developed. The gauge factor of the semiconductor strain gauge was about 46 times larger than that of the traditional metal foil gauge, and the temperature sensitivity was carefully eliminated by temperature compensation. In the range of 10 ~ 100℃, the output drift of the semiconductor strain gauge was reduced by about 30 times (2.5 times of the foil gauge), and the temperature coefficient of the gauge factor was reduced from −0.246/℃ to −0.014/℃.

This balance was calibrated and tested in the Φ0.3 m hypersonic low density wind tunnel, using a HB-2 standard model in a Mach 12 hypersonic flow. The static accuracy of the balance was calibrated better than 0.3% FS. The wind tunnel results have good repeatability of 2.5% FS, and agree generally well with laminar CFD simulations and reference wind tunnel results under similar conditions.

The following are the main observations drawn from this work:

- After careful temperature compensation, the high strain sensitivity of the semiconductor balance is maintained, while the server temperature drift is suppressed.
- The results from the Mach 12 wind tunnel tests show that, the semiconductor balance can be applied to hypersonic aerodynamic experiments.
- The repeatability of C_A is still poor, as compared with C_N and C_{Mz}, and the main reason is suspected to be the temperature gradient effect, requiring further verification and improvement.

Abbreviations

AoA	Angle of attack
C_A	Aerodynamic coefficient of axial force
C_N	Aerodynamic coefficient of normal force
C_{Mz}	Aerodynamic coefficient of pitching moment
D	Forebody diameter
E	Elasticity modulus
F_A	Axial force
F_N	Normal force
GF	Gauge factor
L	Reference length
Mz	Pitching moment
R	Electrical resistance
S	Reference area
a	Average cross-sectional area
l	Length
ε	Strain
v	Poisson's ratio
ρ	Resistivity
π	Piezoresistive coefficient

Acknowledgements
Not applicable.

Authors' contributions
Conceptualization, Yanguang Yang and Huacheng Qiu; Investigation, Huacheng Qiu; Supervision, Yanguang Yang; Writing – review & editing, Huacheng Qiu, Pen Sun and Yanguang Yang; Experiments, Huacheng Qiu, Pen Sun, Genming Chao, Yousheng Wu and Yingdong Chen. All authors read and approved the final manuscript.

Funding
Not applicable.

Availability of data and materials
Not applicable.

Declarations

Competing interests
The authors declare that they have no competing interests.

Received: 26 June 2023 Accepted: 19 October 2023
Published online: 01 December 2023

References

1. Jansen U, Quest J (2007) SG balance improvements are slowing down – Europe can not wait that long. In: Proceedings of the 45th AIAA aerospace sciences meeting and exhibit, Reno, 8-11 January 2007
2. Lynch CS (1999) Strain measurement. In: Webster JG (ed) The measurement, instrumentation, and sensor handbook. CRC Press, Boca Raton
3. Burns DE, Williams QL, Phillips BD et al (2016) Review of potential wind tunnel balance technologies. In: Proceedings of the 10th international symposium on strain-gauge balances, Mianyang, 16-19 May 2016
4. Fleming AJ (2013) A review of nanometer resolution position sensors: operation and performance. Sens Actuat A Phys 190:106–126
5. Qiu H, Min F, Yang Y (2020) Fiber optic sensing technologies potentially applicable for hypersonic wind tunnel harsh environments. Adv Aerodyn 2(1):10
6. Qiu H, Min F, Zhong S et al (2018) Hypersonic force measurements using internal balance based on optical micromachined Fabry-Perot interferometry. Rev Sci Instrum 89:035004
7. Qiu H, Min F, Yang Y et al (2019) Hypersonic aerodynamic force balance using micromachined all-fiber Fabry-Pérot interferometric strain gauges. Micromachines 10(5):316
8. Tomek DM, Sewall WG, Mason SE et al (2006) The next generation of high-speed dynamic stability wind tunnel testing. In: Proceedings of the 25th AIAA aerodynamic measurement technology and ground testing conference, San Francisco, 5-8 June 2006
9. Thomson W (1857) On the electro-dynamic qualities of metals: Effects of magnetization on the electric conductivity of nickel and of iron. Proc R Soc Lond 8:546–550
10. Tomlinson H (1876) On the increase in resistance to the passage of an electric current produced on wires by stretching. Proc R Soc Lond 25:451–453
11. Tomlinson H (1883) The influence of stress and strain on the action of physical forces. Phil Trans R Soc 174:1–172
12. Higson GR (1964) Recent advances in strain gauges. J Sci Instrum 41:405–414
13. Barlian AA, Park WT, Mallon JR et al (2009) Review: Semiconductor piezoresistance for microsystems. Proc IEEE 97(3):513–552
14. Kyowa Electronic Instruments Co Ltd (2020) Kyowa strain gages catalogs, Chofugaoka, Chofu, Tokyo
15. Smith CS (1954) Piezoresistance effect in germanium and silicon. Phys Rev 94(1):42–49
16. Mason WP, Forst JJ, Tornillo LM (1962) Recent developments in semiconductor strain transducers. In: Dean M, Douglas RD (eds) Semiconductor and conventional strain gages. Academic Press, New York
17. Nielsen HA Jr (1985) From locomotives to strain gages. Vantage Press, New York
18. Kulite Semiconductor Products Inc (2011) Kulite strain gage manual. Leonia, New Jersey
19. Damljanović D, Vuković Đ, Vitić A et al (2016) Observations on some transonic wind tunnel test results of a standard model with a T-tail. Sci Tech Rev 66(4):34–39
20. Vuković Đ, Damljanović D (2015) Evaluation of a force balance with semiconductor strain gages in wind tunnel tests of the HB-2 standard model. Proc Inst Mech Eng G J Aerosp Eng 229(12):2272–2281
21. Damljanović D, Rašuo B, Vuković Đ et al (2016) Hypervelocity ballistic reference models as experimental supersonic test cases. Aerosp Sci Technol 52:189–197
22. Bowersox RDW, Schetz JA, Chadwick K et al (1994) Direct measurements of skin friction in hypersonic high enthalpy impulsive scramjet experiments. In: Proceedings of the 32nd aerospace sciences meeting and exhibit, Reno, 10-13 January 1994
23. Novean MG, Schetz JA, Bowersox RDW (1997) Direct measurements of skin friction in complex supersonic flows. In: Proceedings of the 35th aerospace sciences meeting and exhibit, Reno, 6-9 January 1997
24. Goldfeld M, Petrochenko V, Nestoulia R et al (2001) The direct measurement of friction in the boundary layer at supersonic flow velocities. In: Proceedings of the 10th AIAA/NAL-NASDA-ISAS international space planes and hypersonic systems and technologies conference, Kyoto, 24-27 April 2001
25. Brantley WA (1973) Calculated elastic constants for stress problems associated with semiconductor devices. J Appl Phys 44:534–535
26. França DR, Blouin A (2004) All-optical measurement of in-plane and out-of-plane Young's modulus and Poisson's ratio in silicon wafers by means of vibration modes. Meas Sci Technol 15(5):859–868
27. Nathan A, Baltes H (1999) Microtransducer CAD: Physical and computational aspects. Springer Vienna, Wien
28. PLA General Armament Department (2011) GJB 2244A-2011: Specification for wind tunnel strain gage balance. Military Standard Publishing and Distribution Department, Beijing
29. Jiang W, Qiu H, Yang Y et al (2021) High frequency AC electric glow discharge visualization technology and application in big diameter hypersonic low-density wind tunnel. Adv Aerodyn 3(1):14

30. Springer AM (1999) Uncertainty analysis of the NASA MSFC 14-inch trisonic wind tunnel. In: Proceedings of the 37th aerospace sciences meeting and exhibit, Reno, 11-14 January 1999
31. Nagai S, Tsuda S, Koyama T et al (2001) Comparison of winged vehicle force data at large hypersonic wind tunnels. In: Proceedings of the 39th aerospace sciences meeting and exhibit, Reno, 8-11 January 2001

Publisher's Note